Recommendations for efficient and responsible LLM adoption within industrial software development

International Journal of Hydrogen Energy 237 (2026) 155270

Contents lists available at ScienceDirect

International Journal of Hydrogen Energy

journal homepage: www.elsevier.com/locate/he

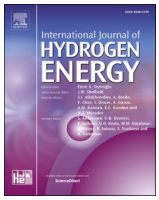

Effects of coal replacement by hydrogen on flame structure, heat release, and NO_x emissions under rotary-kiln iron ore induration conditions

Samuel Colin [a,b,*], Francisco Javier Triana De Las Heras [a], Christian Fredriksson [b], Fredrik Normann [a,b]

[a] Division of Energy Technology, Chalmers University of Technology, 41296, Gothenburg, Sweden
[b] Luossavaara-Kiirunavaara Aktiebolag, Box 952, 97127, Luleå, Sweden

ARTICLE INFO

Keywords:
Hydrogen
Coal combustion
Rotary kiln
Iron ore pelletizing
Flame characterisation
Heat transfer
NO_x emissions
Ignition behaviour
Spectroscopic analysis
Video analysis

ABSTRACT

We investigate the transition from coal to hydrogen in a downscaled industrial burner adapted for hydrogen injection under rotary-kiln conditions. Although replacing coal with hydrogen is an attractive decarbonization route, its effects on combustion behaviour, heat transfer, ignition, flame stability, and NO_x emissions are complex and must be understood before full-scale implementation.

The results show that the largest changes occur when moving from pure coal to 30% H_2 co-firing, with earlier ignition, higher flame stability, and increased temperature. Further increases from 30% to 50% and 70% H_2 cause comparatively smaller changes, suggesting that once co-firing is established, higher hydrogen shares up to 70% do not introduce major additional limitations. NO_x emissions decrease by 38% at hydrogen substitution up to 30%, but then rise sharply with further hydrogen addition, reaching 219% above pure coal under full hydrogen firing. This indicates functional limitations of the tested burner above 50–60% hydrogen substitution.

1. Introduction

Industrial decarbonization of hard-to-abate sectors such are iron and steel, cement, and chemicals, faces a fundamental constraint: processes requiring temperatures above several hundred degrees Celsius that cannot be directly electrified with current technology [1]. Combustion-based systems are therefore expected to persist in those sectors and hydrogen has emerged as primary low-carbon fuel candidate [1–4]. Beyond the specific application, the viability of hydrogen is highly context-dependent, shaped not only by technological maturity and scaling but also by electricity costs and policy instruments such as CO_2 taxation [5–9]. It is attractive in regions where abundant competitive low-carbon electricity and water resources enable cost-efficient electrolysis-based hydrogen production [10–13], particularly when integrated with on-site production systems [10,14]. In the long term, such favourable conditions may be achievable in northern Sweden. In addition to its potential to decarbonize industrial energy use, hydrogen introduces new dimensions of energy system interdependence, which may carry positive implications in certain contexts [4,15].

At the process level, rotary kilns used in iron pelletizing have historically been fired with coal and natural gas. Shifting to hydrogen introduces several process-level risks that warrant careful consideration. This study focuses only on coal to hydrogen transition.

In a rotary kiln the flame serves a dual purpose: it acts as the primary heat source and governs how heat profile is transferred to both the material bed and the kiln wall. This makes the flame's behaviour central to safe and efficient operation. In studied fuel shifting, four important key risks have been identified.

The first concerns heat transfer to the kiln wall. Coal and hydrogen combustion produces a flame with significantly different radiative properties. Co-firing conditions using the same burner can further influence this profile in ways that must be carefully assessed. Reaching pure hydrogen operation may necessitate a fundamental rethinking of burner design, potentially shifting from predominantly radiative toward convection-enhanced configurations. The second risk relates to hydrogen changing ignition behaviour. Hydrogen has a significantly lower ignition energy than coal, on the order of 0.02 mJ compared to several hundred mJ for coal. If ignition occurs too close to the burner, it can accelerate material degradation and shorten burner lifetime, making this a critical parameter to monitor and control. Thirdly, flame stability must be maintained, as uncontrolled fluctuations directly affect the consistency of kiln operation and can compromise product quality.

* Corresponding author. Division of Energy Technology, Chalmers University of Technology, 41296, Gothenburg, Sweden.;
E-mail addresses: samuel.colin@lkab.com, samuelco@chalmers.se (S. Colin).

https://doi.org/10.1016/j.ijhydene.2026.155270
Received 5 February 2026; Received in revised form 9 April 2026; Accepted 24 April 2026
Available online 30 April 2026

The fourth and final risk, and arguably the most pressing given the growing body of literature on the subject, is NO_x emissions. Iron ore rotary kilns operate under inherently hostile conditions from an emissions standpoint [16,17]: large volumes of preheated secondary air at approximately 1200 °C and total air-to-fuel ratios of 4–5. Since post-treatment strategies are either impractical or prohibitively expensive at this scale, primary combustion control remains the most meaningful lever to work with.

Prior work directly relevant to combustion conditions in iron ore rotary kilns remains limited. Two studies conducted at 150 kW scale investigated hydrogen substitution of up to 30%, using either combi-burners [18] or lance injection configurations [19]. In the combi-burner setup, co-firing intensified the flame, promoted earlier ignition and improved stability. NO_x emissions were reduced relative to pure coal and slightly worsen when increasing hydrogen velocity. Total heat transfer to the walls increased in co-firing conditions. Under pure hydrogen operation, heat flux near the burner exceeded that of pure coal but declined to lower values further downstream. Lance injection produced similar effects on flame behaviour, with these effects becoming more pronounced as the separation between hydrogen and coal injection points decreased. Conversely, increasing this distance led to a dramatic rise in NO_x emissions relative to pure coal operation. A separate study further showed that introducing solid particles into a hydrogen flame significantly increases radiative heat transfer compared to pure hydrogen combustion alone [20].

Given the highly specific combustion conditions of the iron ore induration process, it is essential that studies are conducted under representative conditions to yield meaningful insights. Notably, no literature currently exists covering the full transition range from pure coal to pure hydrogen combustion in such conditions. Related work has, however, been carried out for the analogous transition from natural gas to hydrogen. Two studies [21,22] examining the transition from natural gas to hydrogen using a single burner consistently reported a strong increase in NO_x emissions, with one recording a 380% rise under pure hydrogen operation [21]. Heat transfer to the kiln wall was generally reduced under pure hydrogen, while co-firing conditions showed no significant change in the heat transfer profile relative to pure natural gas.

A critical knowledge gap remains in enabling a safe and cost-effective transition from coal to hydrogen. This study addresses experimentally that gap by building on existing 150 kW-scale findings, extending the investigation across the full range of partial coal substitution while maintaining a single burner design already proven at full scale for coal operation.

The study evaluates the impact of this transition on key combustion characteristics, including ignition, axial heat release, flame stability, particle temperature indicator, heat transfer to wall, and NO_x emissions. The overarching objective is to identify critical operational thresholds, define the burner's operable envelope, and characterise the evolution of flame properties throughout the shift from coal to hydrogen.

2. Methods

An experimental approach is prioritised to evaluate operation across the full range from pure coal to pure hydrogen, as the number of parameters influencing flame behaviour in such industrial context is extensive. This provides a more system-level perspective compared to modelling. In large-scale combustion, complex interactions between subsystems and environmental conditions make detailed mechanistic analysis both challenging and costly.

In this study, a limited set of key measurement techniques is employed. Rather than capturing absolute phenomena, these measurements act as indicators of underlying physical changes, enabling a macro-level understanding of flame behaviour. The following sections describe the furnace, experimental setup, and diagnostic methods used to characterise ignition, flame dynamics, heat transfer, and emissions.

2.1. Experimental furnace

The heart of this study comes from the LKAB's Experimental Combustion Furnace (ECF), a facility designed to replicate the temperature and flow conditions found inside an iron-ore pelletizing kiln. The ECF has been used and described in previous work [23–25], providing a well-established platform for industrial combustion research.

The furnace is divided into two main sections: a burner hood and a kiln. The burner hood receives hot secondary air through two inlets, one above called upper inlet and one below the burner, called lower inlet. The kiln section measures 4 m and extends exhaust section including the chimney prolongate the overall furnace to approximately 14 m. Secondary air is preheated externally to temperatures of up to 1050 °C at the burner hood. To mirror the geometry of a full-scale rotary kiln, the ECF outlet is tilted at approximately 3°, and the overall furnace is scaled to one-seventh of its industrial counterpart. Two important simplifications should be noted: the ECF does not rotate, and it contains no product bed to heat, conditions that isolate combustion behaviour from the additional complexity of the pelletizing process itself. A schematic of the ECF, including the axial positions of all measurement ports (P0 to P12), is provided in Fig. 1.

2.2. Burner design and operating conditions

The burner was developed by downscaling an existing full-scale burner and adapted to handle mixed fuel injection from pure coal to pure hydrogen. Coal is delivered through three pipes arranged symmetrically around a central hydrogen injection pipe, ensuring an even distribution of solid fuel. These four fuel pipes are enclosed within a primary air annulus, whose primary role in tested conditions is burner cooling rather than combustion. The primary air flow rate is held constant at 100 Nm^3/h across all cases, corresponding to an exit velocity of roughly 10 m/s, a level at which its jet momentum is negligible relative to the secondary air, coal, and hydrogen flows.

Five fuel mixture cases were investigated, spanning the full range from pure coal to pure hydrogen, with three intermediate co-firing blends at 70/30, 50/50, and 30/70 coal-to-hydrogen energy split. In all cases, the total thermal power was held constant at 510 kW, and the secondary air flow remained fixed at 1900 Nm^3/h, with 60% introduced through the upper inlet. The secondary air entered at a set temperature of 1050 °C (upper) and 1030 °C (lower). During pure coal firing, hydrogen injection was replaced by a 15 Nm^3/h nitrogen flow for safety; during pure hydrogen firing, the transport nitrogen normally associated with the coal flow (10 Nm^3/h) was as well maintained. Full details of the burner operating conditions for each case are given in Table 1.

Fuel properties – The coal used throughout the study was a subbituminous coal with a proximate analysis of 0.4% moisture, 12.8% ash, 18.0% volatile matter, and 68.8% fixed carbon. On an ash-free basis, the ultimate analysis gives mass fractions of 76.7% carbon, 4.1% hydrogen, 4.3% oxygen, 1.5% nitrogen, and 0.3% sulphur, with a lower heating value of 30.473 MJ/kg. The hydrogen supply had a purity exceeding 99.9 vol%, with a lower heating value of 118 MJ/Nm^3.

2.3. Ignition distance and stability diagnostic

To assess how the coal ignition is impacted by hydrogen, an operational camera was positioned at port P0, at the inner edge of the furnace wall. While the camera's settings were not fixed, precluding quantitative analysis on intensity, it provided valuable qualitative insight into ignition behaviour under each fuel condition. Two complementary visualisations were extracted from the footage.

The first is a spatially averaged intensity field, produced by averaging pixel intensities across all recorded frames, after normalising intensity against stable wall temperature zones. This time-mean image enables direct visual comparison of temporal ignition location between cases. The second captures the temporal evolution of the flame through

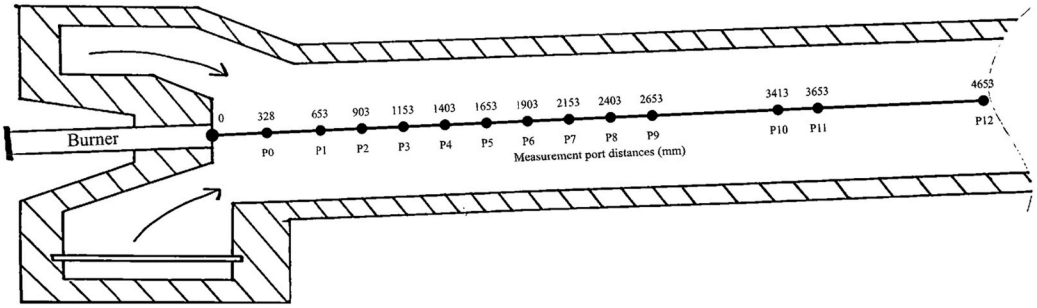

Fig. 1. Schematic of the ECF furnace showing distances from the burner to ports P0–P12. The section has a diameter of 650 mm and a length of 4660 mm, representing a downscaled kiln. The kiln is inclined at 3° relative to the burner. Secondary air enters from the upper and lower sections (arrows), simulating secondary air flow in a full-scale kiln.

Table 1
Burner operating conditions for fuel mixtures, including fuel energy split, coal and hydrogen flow rates and momentum, hydrogen jet exit velocity, burner and total stoichiometric ratios, and primary and secondary air flow rates and temperatures.

Burner configuration Coal/Hydrogen	Unit	100/0	70/30	50/50	30/70	0/100
Total power	kW	510	510	510	510	510
Power coal	%	100	70	50	30	0
Power H_2	%	0	30	50	70	100
Coal flow	kg/h	61	43	30	18	0
Transport air	Nm3/h	10	10	10	10	10
Coal velocity	m/s	25.82	25.82	25.82	25.82	25.82
Coal + transport air momentum	kg·m/s	0.530	0.401	0.308	0,222	0.093
H_2 flow	Nm3/h	0	51	85	119	170
H_2 velocity	m/s	0	250	350	500	833
H_2 momentum	kg·m/s	0	0.32	0.74	1.49	3.54
H_2/coal momentum ratio	-	0	0.79	2.41	6.69	38
Stoichiometry Burner	-	0.22	0.22	0.23	0.24	0.25
Stoichiometry total	-	4.36	4.50	4.62	4.74	4.94
Secondary air flow	Nm3/h	1900	1900	1900	1900	1900
Top secondary air flow	%	60	60	60	60	60
bottom secondary air flow	%	40	40	40	40	40
Top temp. SAF	°C	1030	1030	1030	1030	1030
Bottom temp. SAF	°C	1030	1030	1030	1030	1030
Total primary air flow	Nm3/h	100	100	100	100	100
Primary air velocity	m/s	10.26	10.26	10.26	10.26	10.26
Primary air momentum	kg·m/s	0.37	0.37	0.37	0.37	0.37

vertical and horizontal profiles of maximum intensity. The maximum intensity is extracted along each row and column of the image. These profiles are then stacked in time to form two-dimensional maps that indicates ignition stability and location. The full processing pipeline is illustrated in Fig. 2.

2.4. Coal flame intensity and stability diagnostic

To characterise flame maximum intensity and stability across the full length of the furnace, a CMOS camera (FORGE 5GigE, FG-P5G-50S4C–C) was deployed. Unlike the operational camera, the CMOS camera operated under fixed, controlled settings, enabling both qualitative and quantitative comparisons between cases. It recorded 20-s videos at 114 fps with a resolution of 2448 × 2048 pixels, yielding approximately 2280 frames per measurement. One optical bandpass filter defined two measurement wavelength windows, 543–558 nm and 653–668 nm, and the camera was installed outside the furnace in a water- and nitrogen-cooled probe, with measurements taken sequentially from ports P0 to P9.

Processing began by converting each frame to grayscale, followed by intensity normalization to a reference exposure of 100 μs to ensure comparability across recordings. To visualised at best the intensity and stability change of the coal flame across different mixtures, a method using intensity distribution of high intensity is used. To characterise the intensity distribution statistically, pixels below an absolute threshold of 40 were discarded to limit background information, and the maximum

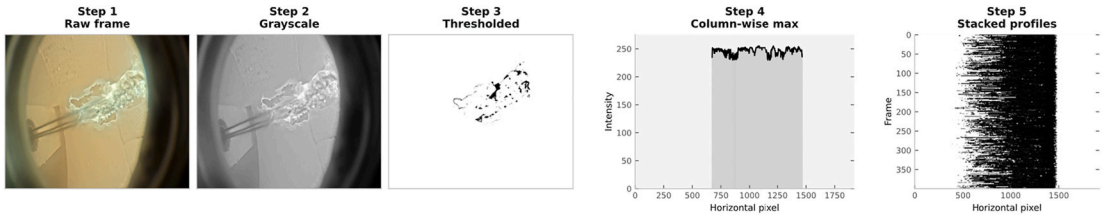

Fig. 2. Step 1 → raw frame; Step 2 → convert to grayscale with wall intensity region correction; Step 3 → extract the maximum intensity; Step 4 → plot maximum intensity per column vs. horizontal pixel position; Step 5 → Convert Step 4 into a single 1D vector per frame, then stack all frames to build the 2D horizontal profile map.

grayscale intensity per row was extracted for each frame. The mean of these row-maximum values was computed for each frame, producing a single temporal signal of flame intensity. Plotting this signal as a probability density function (PDF), with intensity on the horizontal axis and frequency of occurrence on the vertical, provides a compact representation of flame intensity variations across cases and axial positions. The horizontal spread of the distribution reflects the range of intensity levels, while its width serves as an indicator of flame stability. The procedure is illustrated step by step in Fig. 3.

2.5. Coal particle temperature indicator and flame length diagnostic

To gain insight into coal particle temperatures and the extent of the visible flame, optical emission spectroscopy was employed. A spectrometer (Oceanview HR-6XR300-10, 300-line composite blaze grating, 10 μm slit) collected light in the 200–1100 nm wavelength range. Two diaphragms along the line of sight controlled the measurement area to avoid saturation and improve spatial precision. Measurement series was recorded for each port from P0 to P9. Each measurement series comprised 500 spectra recorded with an exposure time of 100 ms, corresponding to a total measurement period of 50 s per port. At each port, the recorded spectrum results from the integration of all radiating elements within a cylindrical measurement volume of a few centimetres in diameter, encompassing both the coal particle field and the furnace wall. Raw spectra were first screened to remove saturated recordings (very few) or those affected by slag buildup at the port. Each valid spectrum was then fitted with a Planck radiation function to extract the so-called line-of-sight temperature. The spectrometer was calibrated using a blackbody oven, yielding an error of approximately 1% at 1000 °C, which decreases with increasing temperature to about 0.3% at 1500 °C. To distinguish the contributions of wall/particles, the location of the average temperature into the normalised minimum and maximum of each series of 500 temperatures in addition to the coefficient of variation (CV) of the extracted temperature was used as a diagnostic indicator. A low CV reflects a measurement dominated by a stable background source either wall radiation or a dense, steady flame. Conversely, a high CV points to significant signal fluctuations caused by intermittent contributions from walls or particles, characteristic of either an ignition zone or a flame tail zone. The axial position at which elevated CV values are recorded determines whether that region corresponds to ignition or flame tail behaviour. The link between CV and measurement location is illustrated in Fig. 4.

2.6. Heat transfer to the wall diagnostic

Two complementary IFRF heat flux probes were used to characterise the thermal loads experienced by the furnace wall. The total heat flux was measured by inserting the probe flush with the inner furnace wall and allowing a stabilisation time of 15 min. The probe consists of a stainless-steel plug instrumented with two Type K thermocouples. The axial temperature gradient between the thermocouples is used, together with a calibration curve, to calculate the combined heat flux from radiation, convection, and conduction reaching the wall surface. The measurement tolerance of the thermocouples follows $\pm 0.0075 \times T$ across the 333–1200 °C temperature range. Alongside the total heat flux probe, a radiative heat flux probe was used to isolate the radiative component. Installed in the same way as the total heat flux probe and allowed to stabilise for 10 min, this probe collects omnidirectional radiation from the furnace and focuses it onto a thermopile sensor, generating a 0–15 mV signal that is linearly proportional to the temperature difference. This signal is then converted to a radiative heat flux value through the probe's calibration curve.

2.7. Gas concentration diagnostic

Flue gas composition was monitored continuously at the furnace outlet, located 4153 mm downstream of the burner. Three analysers operated in parallel at this location: a URAS unit (non-dispersive infrared detection for CO, SO_2, and CO_2), a MAGNOS paramagnetic O_2 analyser, and a LIMAS ultraviolet analyser for NO and NO_2. To assess whether these outlet measurements were representative of conditions further upstream and downstream, radial concentration profiles were also measured using a probe connected to an FTIR and a HORIBA O_2 analyser, traversing across the furnace diameter at axial positions of 2153 mm and 4653 mm. These radial profiles were acquired for all the co-firing cases at 4653 mm and for the 70% hydrogen case at 2153 mm and were measured by traversing both inward and outward, giving 2 values per location. The two values were consistent, and the reported values represent the average of the two passes. A summary of all analysers and their measurement locations is provided in Table 2. All analysers were calibrated prior to the campaign using zero and span gases with known species concentrations.

3. Results

The results structure follows the flame from its origin to its exhaust. Beginning at the burner, the analysis traces how hydrogen co-firing reshapes ignition, then follows the flame downstream to examine its intensity and stability, the evolution of coal particle temperature and density, the redistribution of heat to the furnace wall, and finally the composition of the outlet gases. Together, these four diagnostics described in the Methods build a progressively complete macro picture of what changes as coal is replaced by hydrogen.

Two boundary conditions shape what each diagnostic can see. Camera and spectroscopy both operate in the visible light range, and since pure hydrogen produces no visible light emission, the pure hydrogen case is absent from those analyses and appears only in the gas concentration results. Heat flux measurements were performed for three conditions only: pure coal, 30% H_2, and 70% H_2. Throughout this section, cases are colour-coded for consistency with pure coal in red, and co-firing cases in a blue gradient with progressively lighter shades marking increasing hydrogen fractions from 30% to 70% H_2.

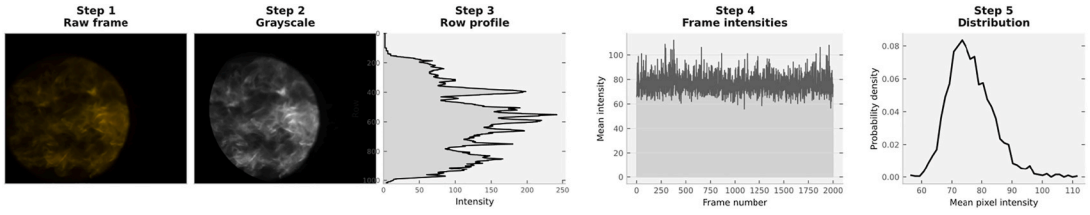

Fig. 3. Raw frame → colour input image; Step 1 → convert to grayscale; Step 2 → extract maximum grayscale intensity per row, discarding pixels below an absolute threshold of 40 to limit background noise (plot: Y-axis: rows - X-axis: intensity); Step 3 → compute the mean of row-maximum values per frame, producing a single temporal signal of flame intensity (plot: Y-axis: intensity - X-axis: frames); Step 4 → plot the signal as a probability density function (PDF), with intensity on the horizontal axis and frequency of occurrence on the vertical axis. (For interpretation of the references to colour in this figure legend, the reader is referred to the Web version of this article.)

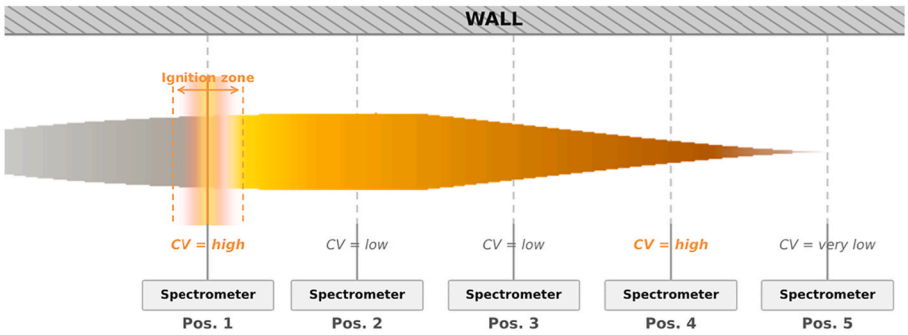

Fig. 4. Schematic illustration of CV distribution along the combustion zone for three flames. High CV values (shown in red) identify regions of strong signal fluctuation associated with the ignition zone or flame tail, while low CV values indicate stable background radiation from the wall or a dense steady flame. (For interpretation of the references to colour in this figure legend, the reader is referred to the Web version of this article.)

Table 2
Gas analysers overview.

Technology	Species	Location
URAS	CO, SO_2, CO_2	Centred at 4153 mm
MAGNOS	O_2	Centred at 4153 mm
LIMAS	NO and NO_2	Centred at 4153 mm
FTIR	H_2O, CO_2, CO, NO, NO_2	Radial measurements in P7 and P12
HORIBA	O_2	Radial measurements in P7 and P12

3.1. *Flame ignition, intensity and stability*

Ignition – Before any quantitative analysis, a typical single raw frame already tells significant information. As illustrated by the three representative frames per case presented in Fig. 5, the most immediate visual effect of hydrogen co-firing is a shift in coal ignition location. In the pure coal flame, light emission originates at the outer edges of the coal jets late within port 0, spreading gradually downstream in a slow, dispersed pattern. Upon hydrogen introduction, combustion activity draws inward and upstream toward the burner centre where hydrogen is injected, although the hydrogen flame itself remains invisible to the camera.

Comparing across co-firing cases, two additional trends emerge. First, at 70% H_2, the coal combustion zone exhibits a noticeably sparse and more homogeneous coal combustion compared to the lower hydrogen fraction cases. Second, prior to ignition, the three coal jets appear undisturbed at 30% H_2, maintaining clear, well-defined, and straight trajectories despite the turbulence induced by the co-flowing hydrogen. At 50% H_2, however, the coal jets show signs of deformation, and at 70% H_2 this effect becomes even more pronounced. This progressive deformation is further evidenced in the video, where the jets can be observed oscillating at 70% H_2.

The early ignition trend is captured qualitatively and quantitatively through the averaged intensity image and the horizontal temporal profile (HTP), both presented in Fig. 6. The HTP tracks the horizontal position of maximum intensity over time, serving as an indicator for both ignition location and its temporal variability. The pure coal flame shows large fluctuations in this profile, reflecting an inherently unstable and later ignition front, giving an averaged pixel location at 996. Among the co-firing cases, the 30% H_2 mixture achieves the earliest ignition at pixel 417. Increasing hydrogen further to 50% and 70%, however, reverses this trend, with a growing ignition distance. Several factors may contribute: higher hydrogen velocities may increase the overall jet momentum, the local O_2 available for coal ignition in high temperature zone may be reduced by hydrogen combustion, and the expansion of the hydrogen flame zone likely generates stronger turbulence and higher

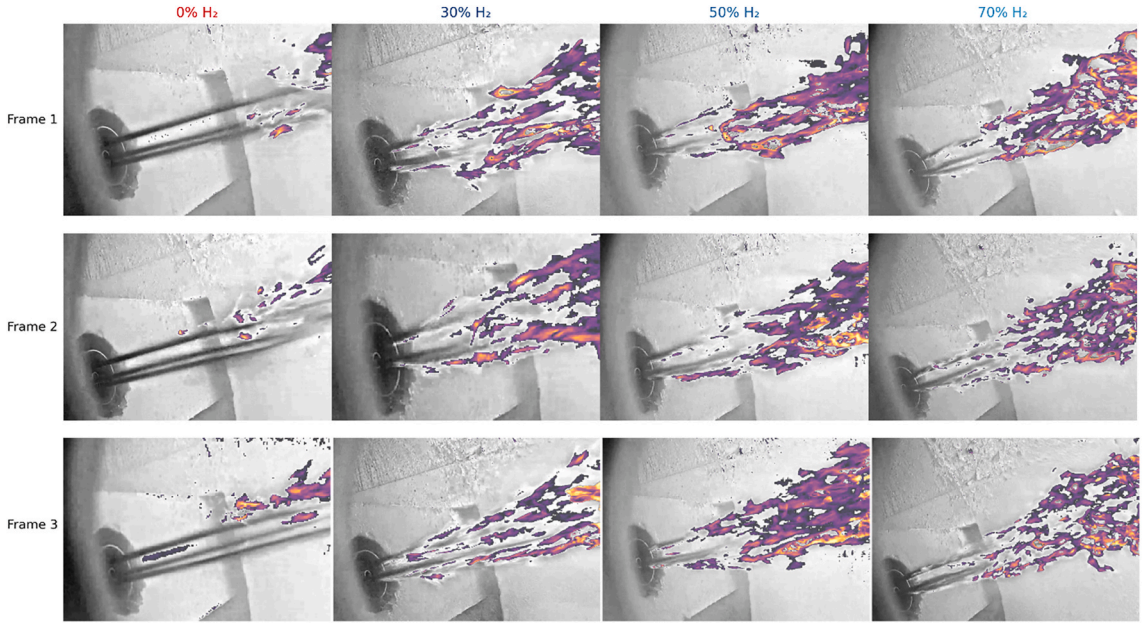

Fig. 5. Typical single-frame images from the operational camera: (a) 100% coal combustion and (b) co-firing with 30% hydrogen and 70% coal. The images are converted to grayscale, and a colormap is applied to highlight high-intensity flame regions for improved visualisation.

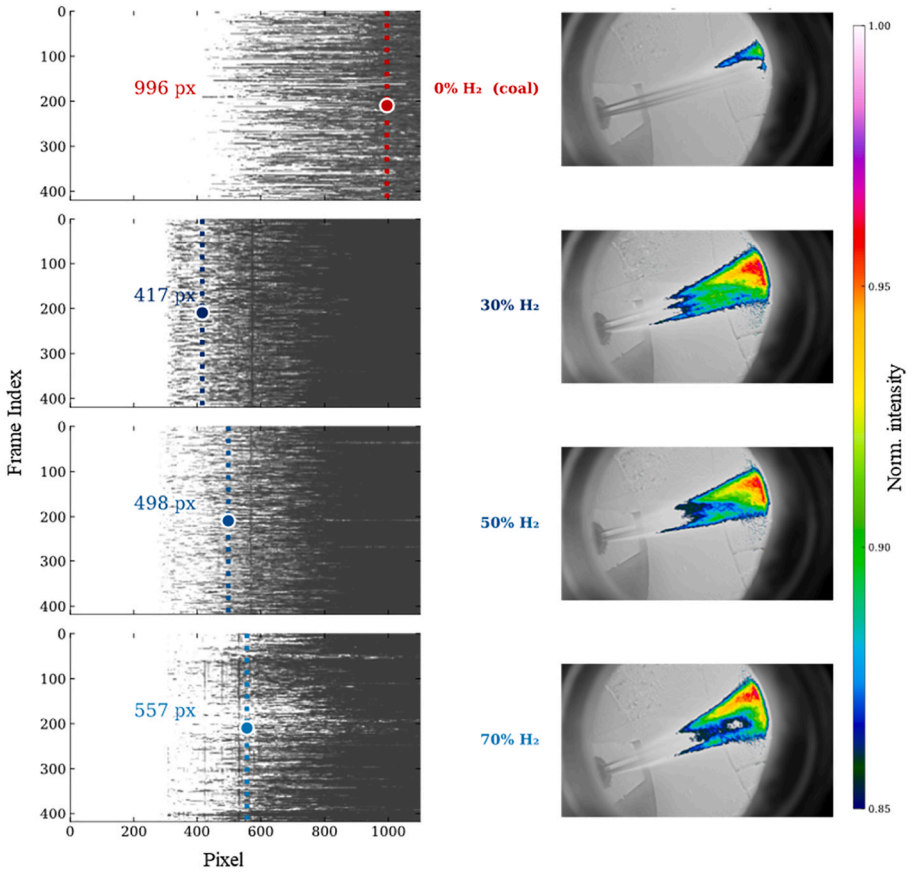

Fig. 6. (a) HTP intensity profiles, where the x-axis shows the horizontal position of the maximum intensity in each row for each frame and the y-axis shows the frame number (time). The dotted line indicates the average pixel position. (b) Average pixel intensity from the operational camera for 0%, 30%, 50%, and 70% coal replacement. Intensities are normalised to 0–1 and corrected relative to the wall intensity. A colour map is applied to the high-intensity region 0.85–1 to highlight intensity gradients. (For interpretation of the references to colour in this figure legend, the reader is referred to the Web version of this article.)

local velocities, compounded by a lower coal particle momentum. The relative contribution of each factor will be examined in the Discussion. The 70% H_2 case additionally exhibits pronounced positional fluctuations in the HTP, which may partly reflect coal mass flow instability during the measurement period.

Intensity and flame stability – Beyond ignition location, hydrogen co-firing transforms the overall character of the flame. Probability distributions of pixel intensity across the ten ports (P0–P9), presented in Fig. 7, tell a consistent observations of increasing intensity and combustion steadiness with hydrogen addition.

In the ignition region (P0–P1), the pure coal flame's intensity at P0 is comparable to background radiation from the heated furnace wall, consistent with the earlier finding that active coal combustion has not yet begun at this location. It is worth recalling here that the CMOS camera observes through the port diameter, capturing a 60 to 80 mm cross-section at the furnace centre, in contrast to the operational camera which is inserted at the inner wall and provides a broader field of view. Within this narrower observation window, all co-firing cases show markedly higher intensity than pure coal at P0. Among them, the 50% H_2 case stands out with a consistently slightly higher intensity than both the lower and higher hydrogen fractions. This is particularly evident at P1, where its narrow intensity distribution points to a notably steady combustion at this early stage. Pixel intensity in these measurements is influenced by the temperature field, the concentration and density of reacting species, exposure time, and observation distance. Since distance is held constant across all cases and exposure time is corrected, two parameters remain as primary variables: coal particle temperature and coal flame density. Coal flame density is expected to decrease with increasing hydrogen fraction, as the coal content diminishes and the turbulence induced by hydrogen progressively disperses the particle field. Against this backdrop, the intensity increase from 30% to 50% H_2 is most plausibly driven by a rise in coal particle temperature. Soot may also play a role, as decreasing O_2 concentration in coal combustion (consummed by hydrogen) create more favourable conditions for soot formation. However, at 70% H_2, temperature gain may appear to be offset by a strongly reduced particle density, explaining why the intensity advantage of higher hydrogen fractions does not continue to grow. The spectroscopic results later lend further indications to both the coal particle temperature trend and the progressive reduction in flame density.

Moving into the main combustion zone (P1–P5 for co-firing, P2–P5 for pure coal), co-firing flames show consistently narrower intensity distributions, that is, more stable in contrast to pure coal that exhibits broader spatial and temporal distributions, reflecting lower combustion stability.

Downstream in the flame tail, the co-firing cases terminate earlier than the pure coal case, with the position following the order of the hydrogen fraction. By P5–P6, the flames are winding down, and by P8–P9, the intensity pattern reflects largely wall temperature more than active combustion. Notably, this residual wall temperature is highest for the 30% H_2 case, followed by 50% and 70% H_2, a pattern later confirmed by the spectrometer and heat flux to wall measurements. The pure coal flame, in contrast, maintains a broad intensity distribution even at the furthest downstream ports, consistent with continued char combustion or glowing residual particles.

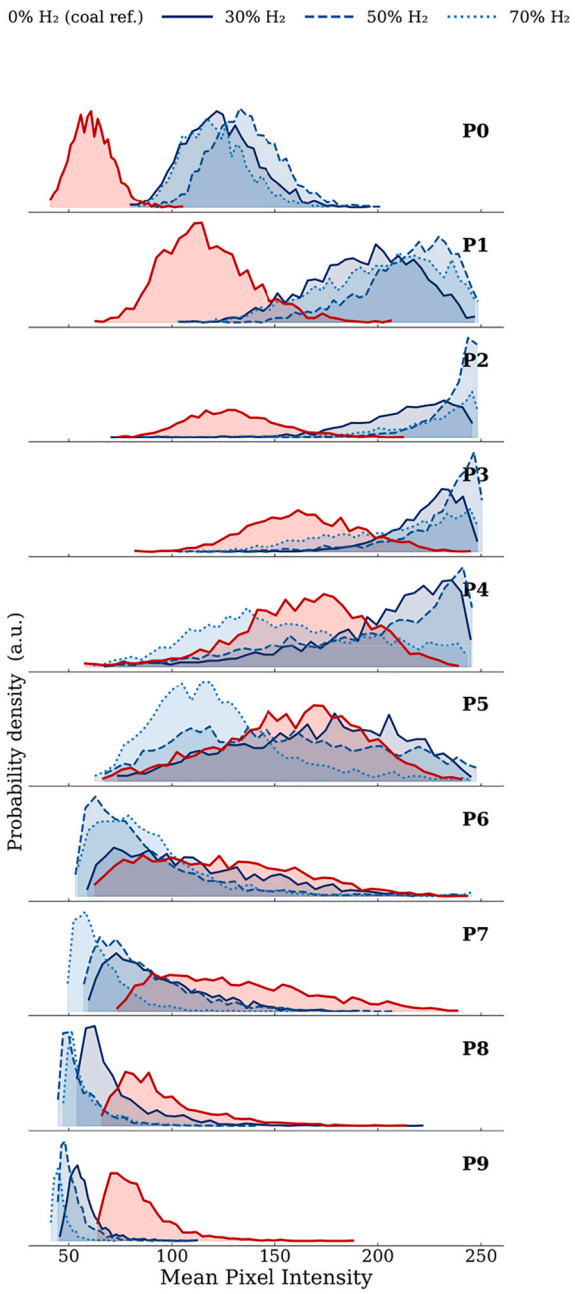

Fig. 7. Probability distributions of the mean maximum-row pixel intensity per frame for all camera ports. Each subplot corresponds to one port (P0–P9), showing filled curves of normalised mean intensity distributions. The colour gradient represents the hydrogen fraction in the fuel mixture (from 0 % H_2 = pure coal to 70 % H_2). Intensity normalization and thresholding were applied to remove exposure-dependent effects and low-signal noise. (For interpretation of the references to colour in this figure legend, the reader is referred to the Web version of this article.)

3.2. Coal particle temperature indicator, flame length and density

Spectrometric line-of-sight temperature measurements offer a further window into how the coal particle field evolves across cases and help reinforce the conclusions drawn from the camera intensity distributions. Fig. 8a presents the line-of-sight temperature together with its minimum–maximum range. Complementary statistics are provided in Fig. 8b, which shows the coefficient of variation, and in Fig. 8c, which shows the normalised position of the average within the minimum–maximum range.

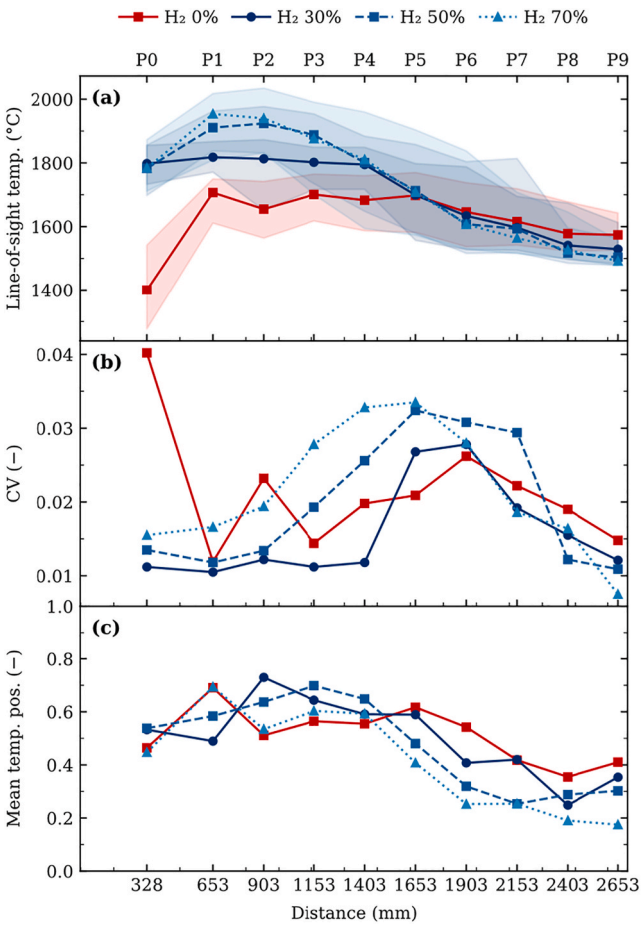

Fig. 8. Statistical analysis of a 500-point line-of-sight temperature series: (a) line-of-sight temperature with min–max shading, (b) coefficient of variation of the line-of-sight temperature, and (c) position of the mean line-of-sight temperature between the normalised minimum (0) and maximum (1). Red represents the pure coal case, while shades of blue indicate co-firing conditions, with lighter blue corresponding to higher hydrogen fractions. (For interpretation of the references to colour in this figure legend, the reader is referred to the Web version of this article.)

A clear hierarchy emerges across the region P0–P5: coal particle field temperature increases progressively with hydrogen fraction. The most dramatic step occurs between pure coal and 30% H_2. A further, important gain follows from 30% to 50% H_2. Beyond this point, the increase diminishes considerably, the 50% and 70% H_2 cases remain very close, with 70% H_2 edging only marginally higher. Much like the pixel intensity from the camera, the line-of-sight temperature derived from the spectrometer is not immune to the influence of flame density. A denser coal particle field contributes more strongly to the integrated signal, while a sparser field gives proportionally more weight to the furnace wall, a cooler background element. The hottest elements tend to dominate the spectral shape because, in the visible range, the Planck function exhibits an exponential dependence on temperature and the spectral peak shifts toward shorter wavelengths as temperature increases. Consequently, the extracted temperature that is based on spectra shape, is biased toward the highest temperatures present within the observed volume, although the relative contributions of all emitting elements still influence the fitted result. In this context, the small gap between the 50% and 70% H_2 cases may partly reflect the lower coal particle density at 70% H_2, which could in reality be somewhat higher than the extracted value suggests.

Coal flame length – The coefficient of variation of the 500-temperature series (CV), presented in Fig. 8b, measures temporal fluctuation

and serves as a useful indicator of both the ignition zone and the flame tail. In the pure coal case, a very high CV at P0 confirms that ignition is occurring at, or just upstream of, the first measurement location. All co-firing cases, by contrast, show low CV values at P0, indicating that ignition is already well underway before the measurement begins. This is fully consistent with the camera findings.

Between P0 and P5, the CV levels across the three co-firing cases follow a clear pattern: the higher the hydrogen fraction, the higher the CV. This likely reflects the progressive reduction in coal particle density from both lower coal flow and higher turbulences. A sparser particle field produces greater fluctuations in the integrated signal. This interpretation is consistent with the camera analysis, where the lower probability density observed for the 70% H_2 case at P0–P1 were attributed to reduced flame density rather than lower particle temperature.

At the downstream end, the onset of the flame tail shifts progressively earlier as hydrogen fraction increases: the 70% H_2 flame ends sooner than the 50% case, which ends sooner than the 30% case. The pure coal flame is a clear outlier; its length and instability make the flame tail difficult to define with precision.

Coal flame density – The normalised position of the averaged temperature within the min-max range of each measurement series provides an additional indicator of coal flame density and is presented Fig. 8c. The closer this value sits to the normalised maximum, the denser the coal combustion is at that location. It is relatively weak in sensitivity and must be interpreted as complement to the information carried by the CV and line-of-sight temperatures.

For all cases, the normalised position follows a broadly similar arc, rising following the ignition zone as combustion intensify and is the densest combustion zone, then declining through the flame tail as the particle field burns out and spread giving more weight for the wall.

Two observations are worth drawing out. First, from port 2 onward, the 50% and 70% H_2 cases exhibit a noticeably smoother profile (similarly than for the CV profiles) compared to both pure coal, which remains the most erratic, followed by the 30% H_2 case. This may reflect a more stabilized, spatially distributed combustion regime, where hydrogen-induced turbulence disperses the coal particles more uniformly and reduces the clustering that drives the sharper fluctuations seen at lower hydrogen fractions and pure coal.

Second, beyond port 5 a clear ordering emerges: the flame tail becomes progressively less dense with increasing hydrogen fraction, reflecting the reduced coal content in each co-firing case as well as a potential acceleration of rate of burning coal particles. Pure coal remains consistently the highest in this region, sustaining a denser, more prolonged combustion tail throughout.

3.3. Heat transfer profile to wall

The shifts in flame behaviour and particle temperature observed across co-firing cases translate directly into a redistribution of heat along the furnace. Fig. 9a presents the total and radiative heat fluxes measured at ports P1, P5, and P7 for pure coal, 30% H_2, and 70% H_2, together with their percentage differences relative to pure coal in Fig. 9b, where the pure coal case serves as the 0% reference line. Second-order polynomial trend lines are added to aid visualisation of the total heat flux profiles.

Across all cases, the total heat flux follows a consistent arc: lowest at P1, peaking at P5, and easing slightly at P7 with a more pronounced decline for co-firing cases. Radiative heat transfer dominates throughout, accounting for 53–74% of the total flux at every port and case.

The effect of co-firing is a change in balance with an upstream increase and downstream decrease in total heat release. At P1, total heat flux increases by approximately +6% relative to pure coal, while at P5 it decreases by around −3%, and at P7 by −10%. The flame delivers more of its energy early and less downstream to the wall. Although very close to the 30% H_2 case, the 70% H_2 case shows the highest total heat flux at P1, this very difference is inverted at P5.

The radiative component tells a more nuanced story. Radiative heat flux gains are substantial across all ports for co-firing with increases of +30–34% at P1, +13–22% at P5, and +6–14% at P7 relative to pure

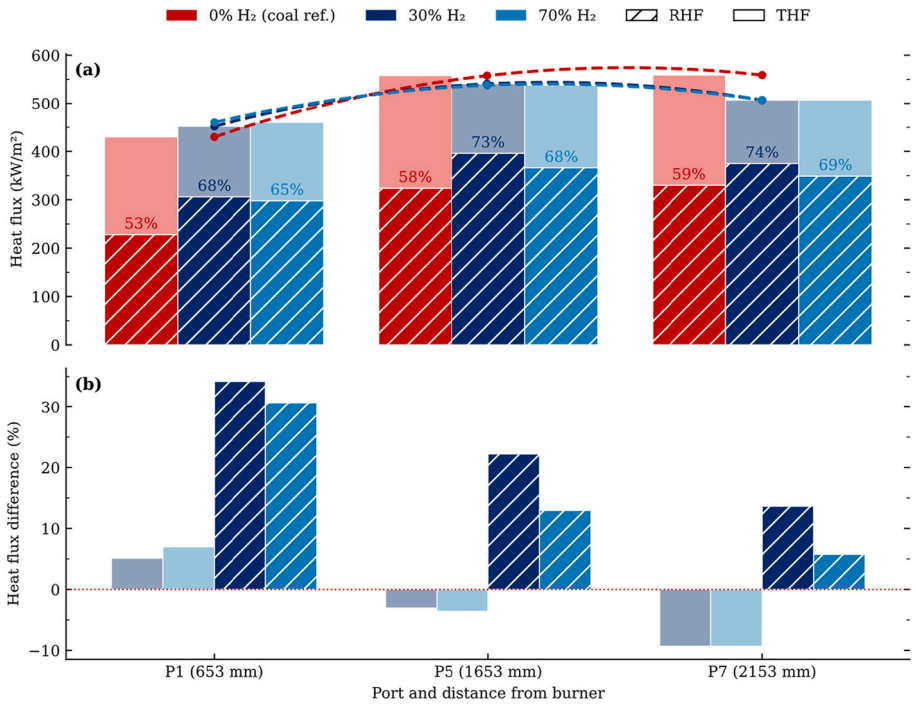

Fig. 9. (a) Total heat flux and radiative heat flux (kW/m^2) at ports 1, 5, and 7 for: pure coal flame (0% H_2 in red), 30% H_2, and 70% H_2. The radiative heat flux is represented by the lined bars, with its percentage contribution to the total heat flux indicated above each bar. (b) Change in total heat flux and radiative heat flux relative to the pure coal case (doted lines at 0). (For interpretation of the references to colour in this figure legend, the reader is referred to the Web version of this article.)

coal. The highest increase is recorded at 30% hydrogen substitution. Crucially, these gains diminish with increasing hydrogen fraction, even as the spectrometer indicates higher coal particle temperatures at higher hydrogen fractions. This apparent contradiction is consistent with the density argument developed earlier: the progressive reduction in coal particle density reduces the total radiation from the flame, offsetting the temperature gain and ultimately dampening the radiative output.

3.4. Emissions

The changes in ignition, fuel mixture, and flame behaviour observed across cases manifest in the outlet concentrations of key species, most notably O_2 and NO. Additional species such as CO_2, CO, and SO_2 primarily act as indicators of coal combustion and coal flow rate, as they originate directly from the coal. In contrast, NO and O_2 represent the most relevant exhaust gas species, with NO being an important atmospheric pollutant and O_2 serving as indication of fuel flows and lambda and being a key concentration parameter for the induration process.

Gas concentrations were measured at a fixed single-point location at 4153 mm downstream of the burner, at the furnace centreline. To contextualise this data, two radial profiles were recorded upstream and downstream of this location: at port P7 (2153 mm) and port P12 (4653 mm) from the burner. All data are presented in Fig. 10, organised as a grid of five rows and three columns, where each row corresponds to one species in the following order: O_2, CO_2, CO, NO, and SO_2. The left and right columns show the radial profiles at 2153 mm and 4653 mm respectively, while the centre column presents the single-point measurements alongside both radial profiles. For all data, the min-max range is added. In the centre column, a slight horizontal offset is applied to each dataset to aid visualisation, with the upstream radial profile positioned earliest, the single-point measurement at the centre, and the downstream radial profile furthest right. All values are reported on a dry basis.

Before interpreting the concentration trends, it is important to acknowledge the limitations of single-point sampling at this location. The exhaust gas is not yet fully radially mixed: at P7, concentration peaks in combustion products are offset from the centreline, reflecting ongoing flame displacement toward the wall. By P12, these peaks have migrated further toward the wall, with O_2 displaying the inverse pattern. Since gas velocities were not measured, velocity-weighted averaging could not be applied, and radial averages therefore represent spatial averages only. The apparent downstream increase in O_2 is an artefact of the non-uniform distribution across streamlines rather than any chemical process, the combustion being completed at P12.

Despite these limitations, the agreement between single-point and radial measurements is satisfactory. Single-point values fall between the upstream and downstream radial averages, with closer agreement to the downstream values as expected given the proximity of the sampling location to P12. At this position, O_2 tends to be slightly underestimated, while CO_2, CO, NO, and SO_2 are slightly overestimated. In response to these findings, the fixed gas sampling location was relocated downstream at 9153 mm in a subsequent experimental campaign, where cross-sectional measurements confirmed radial homogeneity. The same burner was tested in another campaign, and the comparison shows that

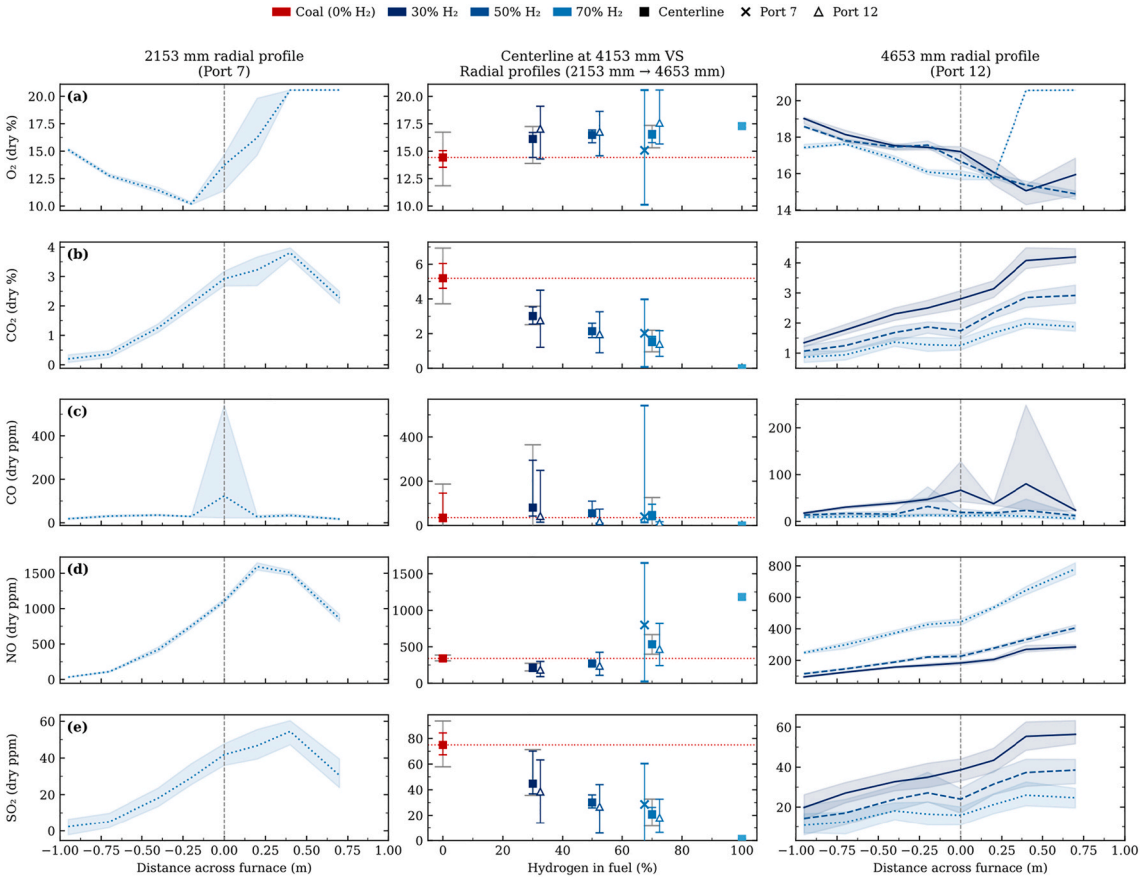

Fig. 10. Radial and centreline gas composition profiles for O_2, CO_2, CO, NO, and SO_2 under varying hydrogen co-firing conditions. Left and right columns show radial distributions at 2153 mm (Port 7) and 4653 mm (Port 12), respectively, with shaded regions indicating min–max ranges. The middle column compares centreline measurements at 4153 mm with corresponding radial data from Ports 7 (filled markers) and 12 (open markers) across hydrogen fractions (0–100%). Error bars represent measurement variability (inner caps), while extended grey caps indicate additional campaign uncertainty. The dashed red line denotes the coal reference level. Red corresponds to pure coal, and shades of blue indicate increasing hydrogen content. (For interpretation of the references to colour in this figure legend, the reader is referred to the Web version of this article.)

the measured NO concentrations are in strong agreement between them. Deviations are mainly observed for CO_2, O_2, and SO_2 in the high-coal cases, particularly for the pure coal condition. In these cases, the longer flame leads to a less uniform radial profile at 4153 mm. The inter-campaign concentration uncertainty is represented in Fig. 10 by grey error bars on the centreline data, shown in addition to the min–max range derived from the radial profiles.

Emission trends across co-firing ratios - CO_2 and SO_2 both decrease with increasing hydrogen fraction, as expected from the progressive reduction in coal combustion, though not in strict proportion to the theoretical coal flow reduction. This non-linearity reflects the localised nature of the single-point measurements, which are increasingly affected by the less uniform radial profiles associated with longer flames, as discussed previously.

CO concentrations remain low throughout and follow a decreasing trend with increasing hydrogen fraction. The notably wide concentration range observed for the pure coal and 30% H_2 cases is likely a measurement artefact: the pure coal data were captured during a particularly stable period of coal flow, while the 30% H_2 measurements coincided with greater feed system instability, a consequence of fluctuations in the coal feed regulation, coal transport and/or burner operation.

The most significant finding concerns NO. At 30% H_2, NO emissions drop considerably relative to pure coal, yet above 50% H_2 NO rise sharply, reversing the initial trend. This bifurcated response demonstrates that the relationship between hydrogen co-firing and NO formation is far from straightforward, and its underlying mechanisms will be explored in the Discussion.

4. Discussion

The discussion is organized into three parts. The first part addresses the measurement techniques and their characteristics. The second part examines the variations in flame profiles and heat transfer behaviour, while the third part focuses on the changes in NO_x emissions.

4.1. Measurement devices

Before entering the physical results discussion, it is essential to clarify the characteristics and limitations of the measurement devices, as these strongly influence the interpretation of the data. Three diagnostic techniques are considered in this discussion: spectroscopic measurements, optical imaging, and radiative heat flux measurements. Only the data analysis methods applied in the present work are discussed here. A schematic overview of the measurement configuration and radiation collection is shown in Fig. 11.

From a geometric perspective, the spectrometer collects light emitted from the furnace over a wavelength range of 200–1100 nm. The collected radiation is integrated radially through the measurement port over an approximate diameter of 1–3 cm. Concerning the camera, the recorded radiation is measured in two narrow wavelength bands, 543–558 nm and 653–668 nm, over a much larger viewing diameter of 60 or 80 cm, depending on the size of the viewing port. This configuration effectively excludes radiation from off-axis angles, meaning that, similarly to the spectrometer, the camera receives light primarily along the radial direction, but over a larger sampled area.

Going to the third measurement device, the radiative heat flux probe is positioned at the furnace wall and measures incident radiation over a hemispherical 2π steradians field of view across a broad wavelength range, spanning from UV to IR. The probe collects radiation within a chamber that is shielded from convective heat transfer. The absorbed radiation heats a thermopile sensor, which responds to the total radiative energy received. As a result, the sensor does not resolve individual wavelength bands but instead measures the heat generated by the integrated radiation over all wavelengths. The measurements are performed after the heat flux signal stabilizes, which typically requires approximately 10–15 min. Once stabilized, the value is recorded as a single measurement and therefore does not represent a temporal average or capture temporal variations. Fast temporal variations are not captured, as the sensor's thermal inertia limits its ability to respond to short-term fluctuations.

A consistent observation when comparing spectrometer measurements with camera observations is that, for all operating conditions, the peak temperature derived from spectroscopy occurs axially upstream of the peak intensity recorded by the camera, typically by one to two measurement ports. This axial shift arises because, although both diagnostics operate within a similar visible wavelength range (approximately 400–700 nm), they measure fundamentally different physical quantities.

The temperature obtained from the spectrometer is determined by fitting the shape of normalised spectral distribution to an apparent blackbody (Planck-law) function. This method emphasizes the relative spectral slope rather than the absolute emitted intensity. In contrast, the camera measures the integrated light intensity, which depends on the radiative power density and is strongly influenced by the concentration of radiating particles, their emissivity, and the effective emitting volume.

In the visible spectral range, the normalised spectral shape is particularly sensitive to the hottest emitting particles due to the exponential temperature dependence of the Planck function at shorter wavelengths. Consequently, even a small fraction of hot, optically thin emitters can dominate the spectral shape used for temperature estimation. Conversely, the camera signal is mainly governed by the total emitted radiant power, which increases with density of radiating particle as well as their temperature level. As a result, the maximum intensity is typically observed further downstream, where soot and char

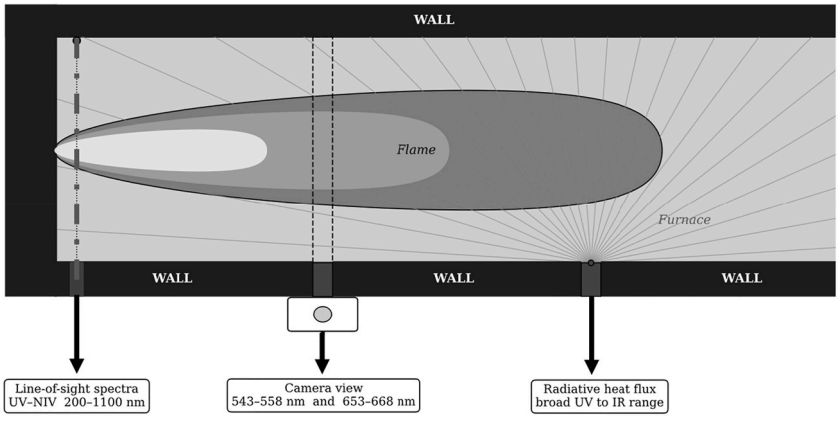

Fig. 11. Schematic representation of spectroscopic, imaging, and radiative heat flux measurement views.

concentrations are higher, even if the local gas or particle temperature is lower.

Additional differences arise from the spatial and temporal averaged sampling characteristics of the instruments. The spectrometer measurements are temporally averaged over a longer exposure time than individual camera frames (100 ms vs. ~8 ms) and integrate light over a few cm^2 into a single value, whereas the camera provides much higher spatial resolution at the pixel level. These differences in spatial and temporal averaging further contribute to the discrepancy observed between spectrometer-derived temperature profiles and camera intensity distributions. Concluding that (1) temperatures derived from the spectrometer represent a spatially and temporally averaged signal from multiple high-temperature sources, with a bias toward higher temperatures. (2) The camera intensity field should not be directly interpreted as a temperature indicator.

Regarding the radiative heat flux, the results show a consistently higher radiative component during co-firing compared with pure coal combustion across all monitored ports (P0, P5, and P7). At port P5, both the camera and spectrometer yield similar results for the pure coal and co-firing cases. However, at port P7, both instruments record significantly lower radiative intensities for co-firing. This apparent contradiction can be explained by the measurement geometry of the radiative heat flux probe. Because the probe measures radiation over a 180° field of view, it captures significant upstream contributions, which are, as showed by camera and spectrometer, more intense under co-firing conditions. In addition, the probe records radiations occurring in the infrared range, which is not detected by either the spectrometer or the camera. These include H_2O radiation from hydrogen and significant portion of wall radiation. Consequently, the probe records a higher total radiative heat flux during co-firing even though the radially line-of-sight observed radiation intensity at P7 is lower.

4.2. Flame profile change

Fig. 12 summarizes the relative changes compared with the pure coal reference case (dotted line at 0%) for three key quantities: flame intensity measured by the CMOS camera, temperature derived from spectroscopic measurements, and the total heat flux at the furnace wall. The evolution of the flame profile is discussed in three stages: (i) ignition behaviour, (ii) the main combustion zone, and (iii) the flame tail.

Ignition – The progressive substitution of coal with hydrogen substantially alters the coal ignition. Both optical imaging and spectroscopic measurements indicate that even small hydrogen additions significantly reduce the distance between the burner and the coal ignition point. The injection of hydrogen introduces additional momentum at the burner outlet and likely modifies the local turbulence field. At 30% hydrogen, the coal jet momentum remains slightly higher than that of hydrogen, with a momentum ratio of approximately 0.8. Under these conditions, the coal jet remains dominant, and the hydrogen jet is likely entrained and mixed into the coal plume. As the hydrogen fraction increases, the momentum ratio shifts in favour of hydrogen, reaching values of 2.4 and 6.7 at 50% and 70% hydrogen, respectively. This means that from a momentum perspective, hydrogen begins to dominate the flow field at 50% blending. The influence of higher hydrogen momentum is visible on the coal jet at the burner outlet as presented in the results from Fig. 5.

Spectroscopic measurements show a temperature increase of approximately 20–30% at port P0, while the camera intensity increases by 200–350% relative to the pure coal case. These observations suggest that the hydrogen flame ignites almost immediately after leaving the burner, providing an early heat source that rapidly heats neighbouring coal particles and promotes their ignition.

When the hydrogen fraction increases beyond 30%, the coal ignition location shifts slightly downstream. The further distance is likely related to the higher hydrogen injection velocity. A higher hydrogen velocity, already significantly greater than that of the surrounding flow at 30% substitution, increases the momentum ratio between the hydrogen jet and its surroundings, thereby enhancing local mixing. This stronger mixing may produce a more confined hydrogen flame with a narrower cone, which may initially interact less and later with the coal particle flow. As a result, the local heat transfer from the hydrogen flame to the coal particles may be slightly reduced compared with lower hydrogen injection velocities. Coal jet velocity before ignition does not appear to be significantly affected by hydrogen addition, with only slightly axially deformation at high hydrogen fraction as discussed previously. This suggests that the hypothesis of constant ignition time with delayed visual ignition due to increased particle velocity is unlikely.

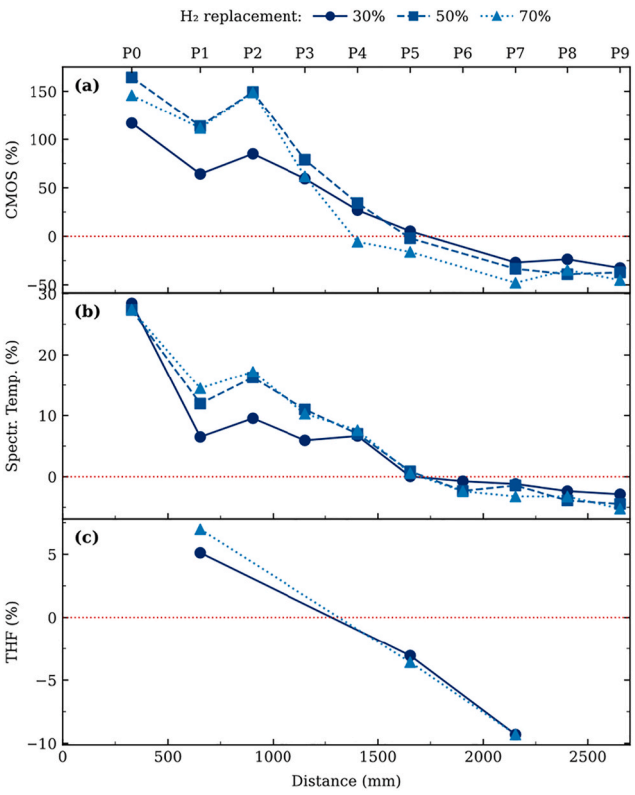

Fig. 12. Relative changes as a function of coal replacement by hydrogen. (a) maximum intensity per port measured by the CMOS camera (%), (b) temperature extracted from the line-of-sight spectroscopic measurements (%), and (c) THF flux relative to the 100% coal (%). All are integrating the pure coal case as baseline (red dotted line at 0%). Port positions (P0–P9) are indicated on the top axis, with corresponding distances (mm) on the bottom axis. (For interpretation of the references to colour in this figure legend, the reader is referred to the Web version of this article.)

Regarding ignition stability, hydrogen addition appears to promote more stable ignition location compared to pure coal case. Higher stability is believed to be associated with the enhanced mixing and consistent heat provided by the hydrogen jets. The velocity gradients between the hydrogen jets, the coal particle stream, and the surrounding air intensify local turbulence, thereby improving fuel–air mixing and creating more favourable ignition conditions. As illustrated in Supplementary Material 1, at and after ignition, the coal flame structure becomes more dispersed in the presence of hydrogen. Coal particles appear more uniformly distributed with stronger turbulences, whereas in the pure coal case, combustion occurs more as a dense particle clusters.

Main Combustion Zone – The main combustion region becomes more compact, stable and intense with increasing hydrogen content, shifting upstream toward the burner. CMOS camera data show a progressive reduction in the difference in intensity between the pure coal and co-firing cases, reaching comparable values at port P6 (1903 mm). While only minor differences are observed between the 50% and 70% hydrogen cases, the most significant change occurs between the pure

coal and 30% hydrogen conditions. The upstream shift of the high intensity region can be attributed to three main factors: (1) a reduced coal feed rate; (2) the higher flame temperature associated with hydrogen combustion; and (3) the turbulence induced by hydrogen injection, which enhances streams mixing and may accelerate reaction rates. Probability density analysis clearly indicates that the presence of hydrogen enhances flame stability not only during ignition but also within the core of the coal flame. This effect is attributed to enhanced mixing, leading to a greater dispersion of coal particles. The increased mixing is further supported by Supplementary Material 1. In addition, spectroscopic and CMOS data indicate that temperature peaks occur closer to the burner and reach higher magnitudes as the hydrogen fraction increases. A non-linearity is observed among cases as the differences among the co-firing cases are significantly smaller than those observed between pure coal and 30% hydrogen.

As shown by Fig. 12c, the change in flame structure leads to a rebalancing of heat transfer. Within ports P0–P4, elevated particle temperatures and hydrogen presence increase both radiative heat fluxes and convective (indicated by total heat flux – radiative heat flux) to the furnace wall. Beyond port P5, for co-firing, the total heat transfer drops below that of the pure coal flame. Nevertheless, as discussed previously, the radiative component remains higher for the co-firing cases at all ports. This suggests that convective heat transfer to the downstream wall decreases under co-firing conditions. It is unfortunately difficult to identify the exact reason for this result, as several parameters may contribute and no available measurements allow one to determine whether one effect dominates over the others. First, flame turbulence may strongly influence the total heat flux. In the presence of hydrogen, the combustion streamlines may not extend to the same location as in the pure coal case. Flame spreading may be reduced, meaning that under co-firing conditions the total heat flux probe is mainly exposed to the secondary air flow. By contrast, in the pure coal case, the wider flame spread may promote stronger mixing near the probe, resulting in a locally higher gas temperature and thus enhanced convective heat transfer. Second, an opposite effect may also arise in the presence of hydrogen. The increased turbulence associated with hydrogen may enhance mixing with the surrounding air, thereby reducing the temperature of the streamlines compared with the pure coal case. Third, the furnace temperature was slightly higher during the pure coal test because of the previous test history. As discussed in the Methods section, these variations reflect the practical fluctuations in boundary conditions that occur in this industrial system. Since the furnace wall contributes significantly to the radiative heat flux, under similar wall conditions the pure coal case would exhibit a lower radiative heat flux, which would in turn result in a lower total heat flux. Finally, because the probe was in contact with the inner wall, the higher wall temperature during the pure coal test may have enhanced conductive heat transfer from the wall to the cooled probe. This may also have contributed to the higher total heat flux measured relative to the co-firing cases.

Flame Tail - In pure coal combustion, the flame tail is long and unstable, as evidenced by both the broad probability density of intensity (P5 to P7) and the more chaotic coefficient of variation measured by the spectrometer. As hydrogen is introduced, the flame progressively contracts: at 30% and 50% hydrogen, the tail shortens and terminates near port P5, while at 70% hydrogen, it recedes further to around port P4. This gradual reduction in flame length, along with a more clearly defined tail end, support the enhanced mixing between the flows, leading to more homogeneous combustion and reducing the persistence of concentrated particle clusters in the downstream region.

4.3. NO_x emissions

The structural transformations of the flame described previously set the foundation for understanding how NO_x emissions evolve as hydrogen progressively replace coal. Temperature field, fuel mixture, mixing between fuels and surrounding air, residence time at high temperature, radical pool and O_2 concentration are all modified, and each plays a role in chemical mechanisms to form NO_x.

Fig. 13 traces the NO_x emissions, expressed in mg per MJ of fuel, as coal is progressively replaced by hydrogen. Rather than a monotonic trend, the data reveals two distinct trends, indicating different balance of competing chemical mechanisms. Before discussing these trends in detail, it is worth noting that the NO_x results indicate a favourable operating range for the burner up to 50% coal replacement.

The decline zone (0–30% hydrogen substitution) - As hydrogen begins to replace coal at 30%, NO_x emissions drops from 784 to 483 mg/MJ, a reduction of approximately 38%. The interpretation of the substantial reduction cannot be attributed to single cause.

Three main overlapping mechanisms are at work in this regime. The first concerns fuel-bound nitrogen (fuel-N), the dominant NO_x precursor under the low-volatile coal conditions typical of iron ore rotary kilns. Each unit of coal displaced by hydrogen removes a fraction of the nitrogen inventory available for conversion to NO_x. Yet this relationship is not proportional: two independent studies [26,27] suggest that a 30% reduction in fuel-N translates to only a 12–17% decrease in NO_x emissions, depending on local combustion temperature and fuel composition. The fuel-N pathway may be therefore a significant contributor, but not the sole architect of the observed decline.

The second mechanism concerns the partitioning of fuel-bound nitrogen between the volatile matter and the char fraction. Hydrogen co-firing raises both the heating rate and the peak temperature experienced by coal particles, accelerating ignition and shifting the volatile-to-char nitrogen balance in favour of volatiles. This mechanism, as reported in the literature, is well supported by several studies [28–30]. The volatile nitrogen species, believed to be primarily HCN for the coal used in this study [31–33] and, to a lesser extent, NH_3, then enter the gas phase where their fate is governed by local conditions. The conversion to NO_x depends mainly on temperature [34], stoichiometry [35], and residence time [36,37]. The enhanced release of nitrogen in the volatile phase may contribute to lowering the background NO_x formed in the hydrogen flame, but its more important effect likely lies in promoting earlier nitrogen release during coal combustion. This, in turn, brings us to the third mechanism: the conversion of char-bound nitrogen to NO_x.

Previous work has shown that char-bound nitrogen is a major contributor to outlet NO_x concentrations [25]. However, char conversion to NO_x is context dependent on O_2 concentration and background NO [38,39]. Both factors favour NO_x reduction in the 30% hydrogen case, due to the lower O_2 concentration and the higher background NO levels. The confirmation of decreasing local oxygen availability from gas concentration measurements at the P12 region and the outlet is not visible as these sampling points sit too far downstream to capture the near-burner chemistry. Although not presented in this study, supplementary measurements conducted near a comparable burner indicated a noticeable decrease in O_2 concentration within the coal combustion zone, consistent with this interpretation and providing indirect support.

A final point concerns the role of OH radicals. OH is involved in key NO formation pathways (e.g., $N + OH \rightarrow NO + H$) and is typically associated with regions of active NO formation [34,40,41]. Under high-temperature and oxidizing conditions, increased OH concentrations can promote NO_x formation. However, under fuel-rich conditions, OH may also contribute to NO_x reduction through interactions with fuel-derived radicals, for example via ($NO + OH \rightarrow HONO \rightarrow NO_2 + H$) [41]. Although OH spatial distribution was not measured in this experimental campaign, it remains an important unknown that may play a role in the observed changes in outlet NO_x levels.

In summary, the approximately 38% NO_x reduction observed at 30% hydrogen substitution is believed to result mainly from few concurrent effects: the increased total thermal NO_x formation (driven by hydrogen combustion) is partially offset by (1) enhanced reduction reactions by both volatiles and char zones with higher background NO_x; (2) the fuel-NO_x pathway is further constrained by reduced oxygen availability during devolatilization; and (3) the lower fuel-N input.

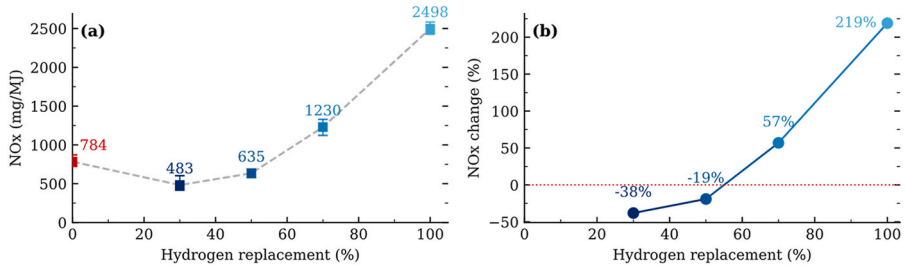

Fig. 13. (a) NO_x emissions (mg/MJ) as a function of the percentage of coal replaced by hydrogen. (b) Change in NO_x emissions relative to the pure coal flame, taken as the 0% reference (dotted line).

The second zone of accelerating rise (30–100% substitution) - Beyond 30% hydrogen substitution, the balance tips decisively. NO_x emissions reverse course and climb steeply, from 483 mg/MJ at the turning point, through a step at 635 mg/MJ at 50% substitution and ending up at 2498 mg/MJ at 100%, ultimately reaching 219% of the pure coal reference. The rise is not gradual but accelerating, suggesting that the mechanisms driving NO_x formation become increasingly self-reinforcing as hydrogen displaces coal.

The dominant driver of this reversal is very likely thermal NO_x formation via the Zeldovich mechanism. Two reinforcing effects conspire to push flame temperatures, and therefore thermal NO_x, to increasingly extreme levels. First, as the coal particle flow diminishes, the thermal buffering capacity of the solid phase is progressively lost; coal particles absorb heat from hydrogen, moderating peak flame temperatures. With fewer particles present, this cooling effect weakens, and the hydrogen flame temperature is likely increasing with each incremental substitution step. Second, at constant hydrogen flow, the growing momentum of the hydrogen jet enhances turbulent mixing, that is likely shortening the flame and concentrating the reaction zone. This mean that along the increasing hydrogen flow, both the concentration of reaction zone and the total hydrogen flame volume is expected to grow. The combination of higher temperatures and a more intense mixing zone creates conditions in which Zeldovich kinetics operate aggressively.

It is worth noting that the reductions achieved in the first act with the coal combustion, seems to offer limited practical benefit if operation in the second act and is likely insignificant at high (>70%) substitution rates. The precise location of the turning point near 30%, and the steepness of the subsequent rise, are themselves depend on factors not fully constrained in this study, including burner geometry, coal type and particle size and the hydrogen injection configuration. The 30% threshold should therefore be interpreted as indicative of the conditions tested here.

5. Conclusion

This study investigated the effects of replacing pulverised coal with central hydrogen injection on flame behaviour, heat transfer, and NO_x formation under conditions representative of industrial rotary kiln pelletizing processes. Experiments were performed in a 510 kW experimental combustion furnace using a burner design that enabled variation of the hydrogen-to-coal energy ratio. Optical imaging, spectroscopic temperature measurements, heat flux probes, and gas analyses were employed to characterise the combustion behaviour and emissions across the full range of fuel substitutions.

The study has shown that co-firing hydrogen with coal promotes earlier coal ignition, increases flame intensity up to 150% upstream and particle temperatures, and shifts the primary reaction zone upstream toward the burner. This restructuring is reflected in the wall heat flux distribution, with stronger near-burner flux increased by approximately 5% and reduced downstream heat transfer to near −10%. Radiative heat transfer dominates and remains above pure coal across all co-firing conditions. Notably, while the transition from pure coal to co-firing produces substantial changes in flame structure and heat transfer, variations among the co-firing cases themselves remain comparatively small, suggesting that once hydrogen is introduced, progressively increasing its share up to 70% substitution does not fundamentally alter the combustion behaviour.

A different perspective emerges for NO_x formation. Two distinct regimes can be identified.

(1) **0–30% H_2**: A monotonic decrease in NO_x (down to −38%), driven by (a) enhanced reduction reactions due to changes in volatile release, (b) reduced oxygen availability during devolatilization, and (c) lower fuel-N input. (2) **30–100% H_2**: An exponential increase (up to +219% at 100% H_2), attributed to enhanced thermal NO formation, overwriting other benefits. While the increase remains moderate up to ~50% substitution, indicating a practical operating window still under pure coal level, beyond this threshold, the exponential rise suggests that burner design and combustion strategies would need to be fundamentally reconsidered to avoid excessive NO_x emissions at higher hydrogen fractions.

CRediT authorship contribution statement

Samuel Colin: Writing – review & editing, Writing – original draft, Visualization, Software, Methodology, Investigation, Formal analysis, Data curation, Conceptualization. **Francisco Javier Triana De Las Heras:** Writing – review & editing, Data curation. **Christian Fredriksson:** Writing – review & editing. **Fredrik Normann:** Writing – review & editing, Validation, Supervision, Resources, Project administration, Funding acquisition, Conceptualization.

Data availability statement

Data related to this work are available from the corresponding author upon reasonable request.

Declaration of competing interest

The authors declare that they have no known competing financial interests or personal relationships that could have appeared to influence the work reported in this paper.

Acknowledgements

The authors gratefully acknowledge the financial support provided by Luossavaara-Kiirunavaara AB (LKAB), the Swedish Energy Agency, and the European Union (EU) under project P2022-00196. The authors also wish to thank Thomas Allgurén (Allguren Energy Engineering Consulting) for managing the in-flame gas sampling measurements.

Appendix A. Supplementary data

Supplementary data to this article can be found online at https://doi.

org/10.1016/j.ijhydene.2026.155270.

References

[1] Hydrogen policy's narrow path: delusions and solutions • energy innovation. Energy Innovation. https://energyinnovation.org/report/hydrogen-policys-narrow-path-delusions-and-solutions/.

[2] Leicher J, Giese A, Wieland C. Electrification or hydrogen? The challenge of decarbonizing industrial (High-Temperature) process heat. J 2024;7(4):439–56. https://doi.org/10.3390/j7040026.

[3] FCA-Report-Decarbonizing-High-Temperature-Heat.Pdf. https://fcarchitects.org/wp-content/uploads/2024/10/FCA-Report-Decarbonizing-High-Temperature-Heat.pdf.

[4] Knorr L, Buchenau N, Schlosser F, Divkovic D, Prina MG, Meschede H. Electrification and flexibility of process heat in energy system modelling: a review. Renew Sustain Energy Rev 2025;216:115698. https://doi.org/10.1016/j.rser.2025.115698.

[5] Arshi O, Mondal S, Gupta YC, Kudapa VK. The hydrogen economy: a review of production, utilization, and impact on the fossil fuel industry. Interactions 2026;247(1):12. https://doi.org/10.1007/s10751-025-02355-z.

[6] Curcio E. Techno-economic analysis of hydrogen production: costs, policies, and scalability in the transition to net-zero. Int J Hydrogen Energy 2025;128:473–87. https://doi.org/10.1016/j.ijhydene.2025.04.013.

[7] Ueckerdt F, Verpoort PC, Anantharaman R, Bauer C, Beck F, Longden T, Roussanaly S. On the cost competitiveness of blue and green hydrogen. Joule 2024;8(1):104–28. https://doi.org/10.1016/j.joule.2023.12.004.

[8] Wei T, Glomsrød S. Cost reduction in low-carbon hydrogen: effective but insufficient to mitigate carbon emissions. Discov Energy 2023;3. https://doi.org/10.1007/s43937-023-00015-3.

[9] Zhang Z, Liu G, Lu X. Supply scale, carbon footprint, and levelized cost assessment of hydrogen production technologies during carbon neutrality transition in China. Energy Strategy Rev 2024;54:101429. https://doi.org/10.1016/j.esr.2024.101429.

[10] Marocco P, Gandiglio M, Audisio D, Santarelli M. Assessment of the role of hydrogen to produce high-temperature heat in the steel industry. J Clean Prod 2023;388:135969. https://doi.org/10.1016/j.jclepro.2023.135969.

[11] Global hydrogen trade to meet the 1.5°C climate goal: trade outlook for 2050 and way forward. https://www.irena.org/-/media/Files/IRENA/Agency/Publication/2022/Jul/IRENA_Global_hydrogen_trade_part_1_2022_.pdf.

[12] Global Hydrogen Review 2023 – analysis. IEA. https://www.iea.org/reports/global-hydrogen-review-2023 (accessed 2026-March-22).

[13] Clean_Hydrogen_Monitor_11-2023_DIGITAL.Pdf. https://hydrogeneurope.eu/wp-content/uploads/2024/11/Clean_Hydrogen_Monitor_11-2023_DIGITAL.pdf.

[14] Pastore LM, Sgaramella A, Bruno G, Lo Basso G, de Santoli L. Coupling high-temperature electrolysis and industrial waste heat for on-Site green hydrogen production: energy, economic and environmental analysis. Int J Hydrogen Energy 2025;126:87–98. https://doi.org/10.1016/j.ijhydene.2025.04.069.

[15] Soudagar MEM, Rao BM, Mohanavel V, Ayyar M, Maranan R, Venkatesh R, Gnanasekaran L, Shanmugapriya D, Santhamoorthy M. Hydrogen-electricity-heat sector coupling: review of integrated models, control strategies, challenges, and future research directions. Renew Sustain Energy Rev 2026;231:116756. https://doi.org/10.1016/j.rser.2026.116756.

[16] Abbas T, Costa M, Costen P, Godoy S, Lockwood FC, Ou JJ, Romo-Millares C, Zhou J. NOx formation and reduction mechanisms in pulverized coal flames. Fuel 1994;73(9):1423–36. https://doi.org/10.1016/0016-2361(94)90057-4.

[17] Wu Z. NOx control for pulverised coal fired power stations. IEA; 2002.

[18] Johansson A, Fernberg J, Sepman A, Colin S, Wennebro J, Normann F, Wiinikka H. Cofiring of hydrogen and pulverized coal in rotary kilns using one integrated burner. Int J Hydrogen Energy 2024;90:342–52. https://doi.org/10.1016/j.ijhydene.2024.09.327.

[19] Colin S, Triana de Las Heras FJ, Normann F, Johansson A, Fernberg J, Sepman A, Wennebro J, Wiinikka H. Configuring hydrogen lancing to reduce carbon and nitrogen oxides emissions from coal-fired rotary kilns. Int J Hydrogen Energy 2025;120:323–32. https://doi.org/10.1016/j.ijhydene.2025.03.322.

[20] Ehlmé E, Gunnarsson A, Andersson K, Normann F. Heat transfer conditions in hydrogen-fired rotary kilns for iron ore processing. Ind Eng Chem Res 2023;62(37):15098–108. https://doi.org/10.1021/acs.iecr.3c02264.

[21] Gee AJ, Smith N, Chinnici A, Medwell PR. Characterisation of turbulent non-premixed hydrogen-blended flames in a scaled industrial low-swirl burner. Int J Hydrogen Energy 2024;49:747–57. https://doi.org/10.1016/j.ijhydene.2023.11.164.

[22] Chishty MA, Katoch A, Saw W, Evans MJ, Medwell PR, Nathan GJ, Chinnici A. Combustion performance, flame structure and EINO scaling of an industrial burner with high excess air fired with natural gas, hydrogen and blends: a numerical study. Appl Energy Combust Sci 2026;26:100475. https://doi.org/10.1016/j.jaecs.2026.100475.

[23] Sepman A, Fredriksson C, Ögren Y, Wiinikka H. Laser-based, optical, and traditional diagnostics of NO and temperature in 400 kW pilot-scale furnace. Appl Sci 2021;11(15):7048. https://doi.org/10.3390/app11157048.

[24] Sefidari H, Ma C, Fredriksson C, Lindblom B, Wiinikka H, Nordin LO, Wu G, Yazhenskikh E, Müller M, Öhman M. The effect of Co-Firing coal and woody biomass upon the slagging/deposition tendency in iron-ore pelletizing grate-kiln plants. Fuel Process Technol 2020;199:106254. https://doi.org/10.1016/j.fuproc.2019.106254.

[25] Edland R, Smith N, Allgurén T, Fredriksson C, Normann F, Haycock D, Johnson C, Frandsen J, Fletcher TH, Andersson K. Evaluation of NOx-Reduction measures for iron-ore rotary kilns. Energy Fuels 2020;34(4):4934–48. https://doi.org/10.1021/acs.energyfuels.9b04091.

[26] Colin S, Normann F, Fredriksson C, Andersson K. Flame characterization of cofiring gaseous and solid fuels in suspensions. ACS Omega 2024;9(26):28268–82. https://doi.org/10.1021/acsomega.4c01770.

[27] Dzurenda L, Hroncová E, Ladomerský J. Extensive operating experiments on the conversion of fuel-bound nitrogen into nitrogen oxides in the combustion of wood fuel. Forests 2016;8(1):1. https://doi.org/10.3390/f8010001.

[28] Czajka KM, Modliński N, Kisiela-Czajka AM, Naidoo R, Peta S, Nyangwa B. Volatile matter release from coal at different heating rates –Experimental study and kinetic modelling. J Anal Appl Pyrolysis 2019;139:282–90. https://doi.org/10.1016/j.jaap.2019.03.001.

[29] Ke X, Engblom M, Cheng L, Chen L, Cai R, Hupa L, Lyu J, Yang H, Zhang M. Modeling and experimental investigation on the fuel particle Heat-up and devolatilization behavior in a fluidized bed. Fuel 2021;288:119794. https://doi.org/10.1016/j.fuel.2020.119794.

[30] Devolatilization Behavior - an overview | ScienceDirect Topics. https://www.sciencedirect.com/topics/engineering/devolatilization-behavior.

[31] Jiao T, Fan H, Liu S, Yang S, Du W, Shi P, Yang C, Wang Y, Shangguan J. A review on nitrogen transformation and conversion during coal pyrolysis and combustion based on quantum chemical calculation and experimental study. Chin J Chem Eng 2021;35:107–23. https://doi.org/10.1016/j.cjche.2021.05.010.

[32] Niksa S. FLASHCHAIN theory for rapid coal devolatilization kinetics. 6. Predicting the evolution of fuel nitrogen from various coals. Energy & Fuels 1995. https://doi.org/10.1021/EF00051A011.

[33] Niksa S. Predicting the evolution of fuel nitrogen from various coals. Symp (Int) Combust 1994;25(1):537–44. https://doi.org/10.1016/S0082-0784(06)80683-1.

[34] Yang F, Xue Q, Zuo H, Wang J. Effects of H2 enrichment on pulverized coal combustion, flame morphology, OH* radicals, CO/CO2 concentration, and NOx in turbulent partially premixed H2/CO-Air flames. Int J Hydrogen Energy 2025;163:150836. https://doi.org/10.1016/j.ijhydene.2025.150836.

[35] Wu S, Che D, Wang Z, Su X. NOx emissions and nitrogen fate at high temperatures in staged combustion. Energies 2020;13(14):3557. https://doi.org/10.3390/en13143557.

[36] Li Y, Sun S, Geng K, Yan P, Feng D, Zhang W, Zhao Y, Yang W. Synergistic activation of reburned char for ultra-low NOx emissions using flue gas recirculation and natural gas in a 10 kW furnace. J Environ Manag 2025;373:123614. https://doi.org/10.1016/j.jenvman.2024.123614.

[37] Li D, He X, Peng X, Chen C, Li Z. Experimental study and CFD modeling of NOx reduction and reductive gas formation in deep reburning of cement precalciner. Fuel Process Technol 2022;229:107183. https://doi.org/10.1016/j.fuproc.2022.107183.

[38] Chaiklangmuang S, Jones JM, Pourkashanian M, Williams A. Conversion of volatile-nitrogen and char-nitrogen to NO during combustion. Fuel 2002;81(18):2363–9. https://doi.org/10.1016/S0016-2361(02)00175-8.

[39] Molina A, Murphy JJ, Winter F, Haynes BS, Blevins LG, Shaddix CR. Pathways for conversion of char nitrogen to nitric oxide during pulverized coal combustion. Combust Flame 2009;156(3):574–87. https://doi.org/10.1016/j.combustflame.2008.11.012.

[40] Wei L-M, Chen Y-F, Yao N-N, Xu Q-Y, Zhang J-K, Huang Y, Pan W-G. Combustion characteristics and NOx formation mechanisms of ammonia/methane blended fuels: a review. Int J Hydrogen Energy 2025;155:150349. https://doi.org/10.1016/j.ijhydene.2025.150349.

[41] Li Z, Zhang W, Chen Z, Ren Z, Ning S, Li M. A kinetics mechanism of NOX formation and reduction based on density functional theory. Sci Total Environ 2023;867:161519. https://doi.org/10.1016/j.scitotenv.2023.161519.

Supplementary Material 1: Visualization of turbulence based on 10 raw frames at Port 0.